Helicon waves in the magnetotail

G. S. Lakhina,[1] A. S. Sharma,[2] and K. Papadopoulos[2]

[1]   The helicon modes are studied in Earth's magnetotail using the Harris sheet as a model of its equilibrium. The plasma sheet is divided into two regions: In region 1 both the electrons and the ions are treated as magnetized, whereas in region 2 the electrons are treated as magnetized but the ions are unmagnetized. The eigenmode equation for the low-frequency, parallel propagating right-hand polarized modes is solved for the two cases, namely, (1) the uniform regions and (2) the inhomogeneous case. The eigenvalues and the eigenfunctions are obtained for the symmetric and antisymmmetric helicon modes. The case of uniform regions predicts lower frequencies for both the symmetric and antisymmetric modes than that of the inhomogeneous case. For typical plasma sheet parameters, the wave frequencies are found to be in the range of $\sim(1-50)$ mHz for the symmetric modes, and $\sim(5-100)$ mHz for the antisymmetric helicon modes. The wavelengths (along x direction) associated with the helicon modes are in the range of $\sim(0.3-9)$ R_E. The antisymmetric mode does not allow flux crossing across the neutral sheet axis. The symmetric helicon mode does allow flux crossing leading to the change in the magnetic topology, and thus, it must involve reconnection.

1.   Introduction

[2]   There are several observational and theoretical studies on the existence of low-frequency MHD waves in the ULF-ELF frequency range in the magnetotail of the Earth's magnetosphere [*Russell*, 1972; *Tsurutani et al.*, 1987; *Siscoe*, 1969; *McKenzie*, 1970; *Lee et al.*, 1988; *Lakhina et al.*, 1990; *Verheest and Lakhina*, 1991; *Kalra and Lakhina*, 1993; *Bauer et al.*, 1995; *Fruit et al.*, 2002a, 2002b; *Sharma et al.*, 2008]. Many mechanisms, including those based on Kelvin-Helmholtz and ballooning mode instabilities have been proposed for the excitation of the low-frequency MHD waves. Such long-wavelength, low-frequency waves can transport energy from one part of the magnetosphere to another, and therefore their generation and propagation in the magnetosphere are of practical interest. For example, the thermal catastrophe model of the substorm is essentially based on the resonance absorption of the Alfvén waves which are coming from the magnetopause boundary into the plasma sheet region [*Smith et al.*, 1986; *Harrold et al.*, 1990].

[3]   Conventionally, the ULF waves have been studied using the MHD approach which is usually sufficient in most parts of the magnetotail as the wave phenomena involve low frequencies (much smaller than the ion gyrofrequency, Ω_i) and long wavelengths (as compared to ion gyroradius, ρ_i) [*McKenzie*, 1970; *Kalra and Lakhina*, 1993; *Fruit et al.*,

2002a, 2002b, 2004]. Recently, *Louarn et al.* [2004] have shown that the magnetic field fluctuations of the plasma sheet having periods $\sim$20 s observed by Cluster during and just after the substorm onset are compatible with the MHD eigenmodes of the sheet [*Fruit et al.*, 2004]. However, close to the neutral sheet (where the magnetic field can become either zero or very small during the growth phase of the substorm), the ion response becomes essentially unmagnetized and the MHD approach, which treats both the ions and the electrons to be magnetized, breaks down completely. Hence the nature of the wave mode is expected to change in the neutral sheet region. Under the MHD approximation, the low-frequency modes are of three types, namely, the shear Alfvén modes and the slow and fast magnetosonic modes. If one considers the waves propagating parallel to the magnetic field, B_0, the dispersion relation for the right-hand polarized waves, under the approximation $\omega \ll \Omega_i$, gives the Alfvén modes. In this case the ion Hall current completely cancels the electron Hall currents, and the wave is maintained by the ion polarization current. However, when the ions are unmagnetized, the electron Hall currents cannot be neutralized by the ions (as they do not have any Hall current), and one gets the Helicon wave [*Aigrain*, 1961; *Konstantinov and Perel*, 1960; *Papadopoulos et al.*, 1994; *Zhou et al.*, 1996]. Therefore, it is interesting to investigate the propagation characteristic of Alfvén waves coming from the magnetopause and crossing the neutral sheet.

[4]   It has been pointed out that helicon waves may lead to the fast current and flux penetration across the neutral sheet [*Papadopoulos et al.*, 1994]. Some other application of the helicon waves could be the generation of field-aligned currents and magnetic flux ropes. The field-aligned current

---

[1]Indian Institute of Geomagnetism, Navi Mumbai, India.
[2]Department of Astronomy, University of Maryland, College Park, Maryland, USA.
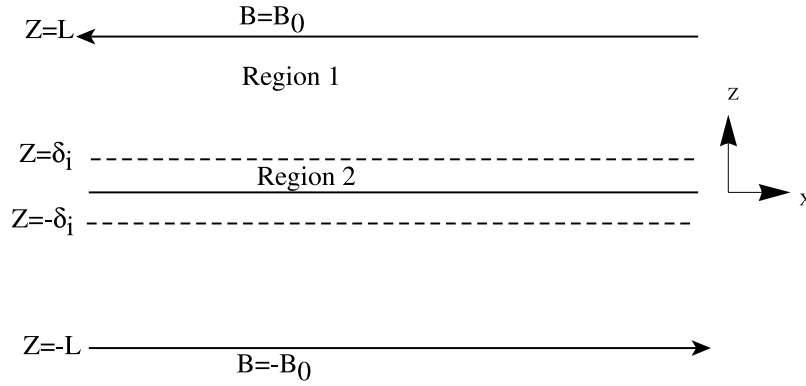
Figure 1. Schematic diagram for the Earth's magnetotail. The plasma sheet extends from $z = -L$ to $z = +L$. The portion enclosed by the dashed lines is region 2, and it extends from $z = -\delta_i$ to $z = +\delta_i$. The rest of the plasma sheet is denoted by region 1. In region 1, both the electrons and the ions are magnetized, whereas in region 2 either both are unmagnetized (i.e., two uniform region case) or only the electrons are magnetized but ions are unmagnetized (i.e., inhomogeneous case). The magnetopause boundary will be at $z = \pm\lambda$ (not shown here).

is produced as a consequence of the closure of the helicon waves current (which lies in the plane transverse to $\mathbf{B}_0$). The large-amplitude helicon wavefields could give significant twist in the original magnetic field, thus producing flux ropes.

[5] Recently, *Lakhina and Tsurutani* [1997] and *Lakhina* [2001] have studied the helicon mode instability driven by an anisotropic, ionospheric-origin oxygen ion beam in the plasma sheet region. In their model, the presence of oxygen ions in the plasma sheet region results in only partial cancellation of the electron Hall current, thus leading to the occurrence of helicon modes rather than the Alfvén modes. The helicon modes can be easily excited when the long-wavelength firehose modes are stable. The helicon modes are likely to attain saturation as the typical e-folding time of the instability is about a few minutes in the near-Earth plasma sheet region. Therefore, the instability could significantly affect substorm dynamics and lead to enhanced ionosphere-magnetosphere coupling. Low-frequency turbulence produced by these modes could scatter electrons trapped in the inner central plasma sheer region and help excite the ion tearing modes, leading to substorm onset. As a result, the oxygen ions would be injected into the Earth's nightside magnetosphere. Repeated injections by this process would lead to enhanced oxygen ion fluxes in the storm-time ring current [*Lakhina*, 2001].

[6] In section 2 we describe the model, derive the wave equation, and discuss its solution for the symmetric and antisymmetric helicon modes. Section 3 deals with the application to the magnetotail, and section 4 gives the conclusions.

2. Magnetotail Model

[7] We consider a one-dimensional Harris sheet model for the magnetotail with the magnetic field $\mathbf{B} = B_0 \tanh(z/L)\mathbf{x}$, where L is the half thickness of the plasma sheet (see Figure 1). We divide the magnetotail in two regions. Region 1 (or the outer region) extends from $|z| \geq \delta_i$, and region 2 (i.e., the inner region centered around $z = 0$) with $|z| \leq \delta_i$, where $\delta_j = (\rho_j L/2)^{1/2}$, with $\rho_j = V_{tj}/\Omega_{0j}$, $V_{tj} = (2T_j/m_j)^{1/2}$, and $\Omega_{0j} =$

(eB_0/m_jc) as the gyrofrequency of the charged particle with respect to the asymptotic magnetic field value (i.e., the lobe field). Here the subscripts are as follows: $j = e$, electrons; $j = i$, ions. The magnetopause position is taken as $z = \pm\lambda$.

[8] Our choice of partitioning the magnetotail into two regions is based on the properties of the particle orbits in the Harris-sheet-like configurations as discussed by *Dobrowolny* [1968] while studying the tearing instability of a neutral sheet. It is found that in the region $\delta_j < |z| < |\lambda|$ (i.e., region 1 here) the particles execute Larmor radius orbits around the magnetic field lines and they do not cross the neutral plane $z = 0$ (i.e., noncrossing particles). In the region $|z| < \delta_j$ (i.e., region 2 here) the particles move freely and are reflected from the magnetic mirrors at the points $z = \pm\delta_j$. These particles have straight line orbits and they cross the $z = 0$ plane during their motion (i.e., crossing particles) [*Dobrowolny*, 1968].

[9] Consequently, for our case, region 1 is an adiabatic region where both the electrons and the ions are fully magnetized. In region 2, which corresponds to $|z| < \delta_i$, the ions are essentially unmagnetized (i.e., they have straight line orbits crossing the null plane ($z = 0$)) but the electrons are treated as magnetized. In fact, for the Harris sheet model, in a very thin region, $z < \delta_e$ centered at $z = 0$, even the electron motion would become unmagnetized for any nonzero wave frequency, ω, unless a finite B_z or B_y component is present. However, for simplicity, we do not consider this thin electron diffusion region. This is the usual equilibrium while studying the tearing modes in the magnetotail [*Zelenyi and Kuznetsova*, 1984; *Lakhina and Schindler*, 1988; *Lakhina*, 1992]. We use two-fluid equations to describe the dynamics of the charged particles in the magnetotail. We consider the perturbations to be of the general form $g = g(z) \exp[ikx - i\omega t]$. From the linearized equations of motion and continuity of electrons and ions, along with Maxwell's equations, the wave equation for the right-hand polarized modes can be derived as

$$\left(\frac{d^2}{dz^2} - k^2 + \frac{\omega^2}{c^2}\right)E = \frac{\omega_{pe}^2\,\omega E}{c^2(\omega - \Omega_e)} + \frac{\omega_{pi}^2\,\omega E}{c^2(\omega + \Omega_i)}, \quad (1)$$

where $\omega_{pj} = (4\pi n_0(z)e^2/m_j)^{1/2}$, and $\Omega_j = (eB(z)/m_jc)$ are the local plasma frequency and the gyrofrequency of the jth species, respectively, and $E = (E_y - iE_z)$ is the electric field of the right-hand polarized wave. We shall consider the low-frequency waves which satisfy $\omega^2 \ll \Omega_{0i}^2$ such that throughout in region 1, $\omega^2 \ll \Omega_i^2$, but in region 2, $\Omega_i^2 \ll \omega^2 \ll \Omega_e^2$. Under the above scaling, the equation for E in region 1 is

$$\frac{d^2 E_1}{dZ^2} - \left[b^2 - a^2 \frac{n(Z)}{n_0} \frac{B_0^2}{B^2(Z)}\right] E_1 = 0, \qquad (2)$$

and in region 2 it is

$$\frac{d^2 E_2}{dZ^2} - \left[b^2 - R\,a\,\frac{n(Z)\,B_0}{n_0\,B(z)}\right] E_2 = 0, \qquad (3)$$

where $Z = z/L, b = kL, a = (\omega L/V_A), R = L/d_i$, where $d_i = c/\omega_{pi}(0)$ $\omega_{pi}(0)$ is the ion skin depth, and $V_A = (B_0^2/4\pi n_0 m_i)^{1/2}$ is the constant Alfvén velocity defined with respect to the asymptotic magnetic field and the number density at the neutral axis. Before considering the Harris sheet model, we consider a much simpler case where both regions 1 and 2 are treated as homogeneous but with different values of the magnetic fields and plasma densities. This approach is simple and amenable to complete analytical solution, thus providing a better insight of the physical mechanisms involved. This methodology has been used in several papers dealing with the excitation of low-frequency electromagnetic modes in the magnetotail [e.g., *Siscoe*, 1969; *McKenzie*, 1970; *Lee et al.*, 1988; *Kalra and Lakhina*, 1994].

2.1. Case of Uniform Regions

[10] We consider all the equilibrium quantities in regions 1 and 2 as uniform and denoted by the subscripts 1 and 2, respectively. In this case the coefficients of the differential equations (2) and (3) are constants, and the solutions for E can be written as

$$E_1 = C_1 \exp[-K_1 Z] + C_2 \exp[K_1 Z], \qquad (4)$$

$$E_2 = g_1 \exp[-K_2 Z] + g_2 \exp[K_2 Z], \qquad (5)$$

where $K_1 = (b^2 - f_1 a^2)^{1/2}$, and $K_2 = (b^2 - f_2 aR)^{1/2}$ with $f_1 = n_1/n_2$ and $f_2 = B_1/B_2$. Here n_1 (n_2) and B_1 (B_2) are the number density and the magnetic field in region 1 (region 2), respectively. We shall use the following boundary conditions:

$$Z = \bar{\lambda}: \quad E_1(Z = \bar{\lambda}) = C_0; \quad E_1'(Z = \bar{\lambda}) = 0, \qquad (6)$$

$$Z = 0: \quad E_2(Z = 0) = g_0; \quad E_2'(Z = 0) = 0,$$
$$\textit{(symmetric mode)}, \qquad (7)$$

and

$$Z = 0: \quad E_2(Z = 0) = 0; \quad E_2'(Z = 0) = g_0,$$
$$\textit{(antisymmetric mode)}. \qquad (8)$$

Then, using the boundary conditions (6) and (7), the solutions for E_1 and E_2 for the symmetric case can be written as

$$E_1 = C_0[\exp[K_1(\bar{\lambda} - Z)] + \exp[-K_1(\bar{\lambda} - Z)]]/2, \qquad (9)$$

$$E_2 = g_0[\exp[-K_2 Z] + \exp[K_2 Z]]/2, \qquad (10)$$

Matching the above two solutions at $Z = \bar{\delta}_i$ yields the dispersion relation for the symmetric mode,

$$K_1 \tanh[K_1(\bar{\delta}_i - \bar{\lambda})] = K_2 \tanh[K_2\bar{\delta}_i], \qquad (11)$$

and determines C_0 in terms of g_0 (or vise versa), thus completely specifying the behavior of E in the entire region with

$$C_0 = \frac{\cosh[K_2\bar{\delta}_i]}{\cosh[K_1(\bar{\delta}_i - \bar{\lambda})]} g_0 \qquad (12)$$

We have checked and solved the dispersion relation using Mathematica, and the numerical results are shown in Figures 2a and 2b for fixed values of f_1 and f_2 and for some values of the parameter R. Figure 2a is for $\bar{\lambda} = 1$, and Figure 2b is for $\bar{\lambda} = 2$. One can clearly see from Figure 2 that the dispersion relation departs considerably from that of the local Alfvén mode dispersion relation in region 1, given by $\omega_A = kV_A$, with magnetic field B_1 and number density N_2 (cf. long dashed curve at the top) for all values of R. The dashed curves are for the local helicon wave dispersion relation in region 2, given by $\omega_H = (k^2 c^2/f_2 \omega_{pe}(0)^2)\Omega_{0e}$, for different values of R. For a given R, the computed wave frequencies are higher than the helicon wave frequency at a given k. Figure 3 shows the structure of the normalized eigenfunction $E(z) = E/g_0$ for the mode. The wave functions $E[z]$ shown in Figures 3a and 3b correspond to the case of $\bar{\lambda}$ = 1 and 2, respectively. We note that $E(z)$ (which is more or less insensitive to the variation of R from 1 to 50) increases smoothly as the neutral sheet is approached and it peaks at z = 0. The shape of $E(z)$ curves remains nearly the same for both the cases of $\bar{\lambda}$ = 1 and 2.

[11] From (5) and (8), the solutions for E_2 for the antisymmetric mode can be written as

$$E_2 = \frac{g_0[-\exp[-K_2 Z] + \exp[K_2 Z]]}{2 K_2}, \qquad (13)$$

Matching E_1 solution given by (9) and the solution for E_2 given by (13) at $Z = \bar{\delta}_i$ yields the dispersion relation for the antisymmetric mode,

$$K_1 \tanh[K_1(\bar{\delta}_i - \bar{\lambda})] = K_2 \coth[K_2\bar{\delta}_i], \qquad (14)$$
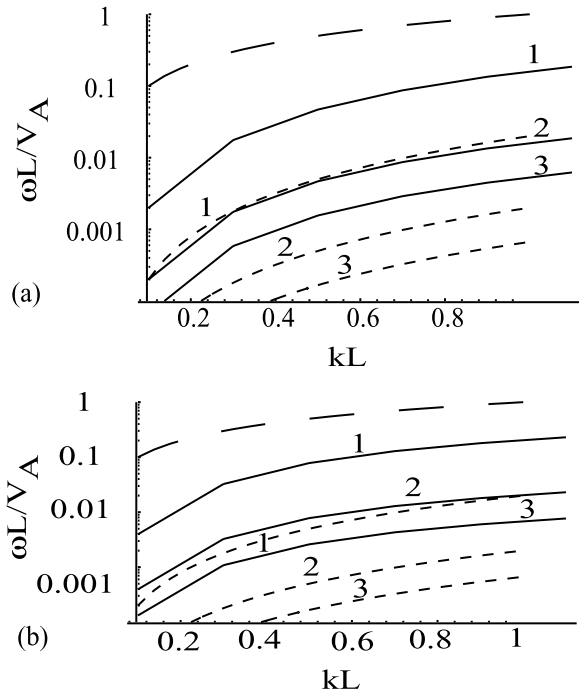
Figure 2. Variation of $a = (\omega L/V_A)$ versus $b = kL$ for the symmetric mode in two uniform region case with $f_1 = n_1/n_2 = 0.1$, $f_2 = B_1/B_2 = 50$, and $\bar{\delta}_i = 0.1$, and for $R = L/d_i = 1$, 10, and 30 for the solid curves 1, 2, and 3, respectively. The long-dashed curve is for the local Alfvén mode dispersion relation in region 1 but with density n_0, and the dashed curves 1, 2, and 3 are for the local helicon mode dispersion relation, ω_H, in region 2 for $R = 1$, 10, and 30, respectively. The dispersion relation for (a) $\bar{\lambda} = 1$ and (b) $\bar{\lambda} = 2$ is shown. The frequencies lie between the Alfvén wave, ω_A, and helicon wave, ω_H, frequencies.

and determines C_0 in terms of g_0 (or vise versa) as before,

$$C_0 = \frac{\sinh[K_2\bar{\delta}_i]}{K_2 \cosh[K_1(\bar{\delta}_i - \bar{\lambda})]} g_0 \qquad (15)$$

Figure 4a (for $\bar{\lambda} = 1$) and Figure 4b (for $\bar{\lambda} = 2$) show the dispersion relation for the antisymmetric mode for various values of R. The characteristics of the dispersion curves do not change significantly when $\bar{\lambda}$ changes from 1 to 2 as seen from Figures 4a and 4b. It is clear from Figures 4a–4b that the eigenfrequencies for the antisymmetric mode are of the same order or higher than that given by the local dispersion relation for the Alfvén mode (cf. long dashed curve), but these are much higher that those of local helicon waves in region 2 (dashed curves). Figure 5 shows the normalized eigenfunction $E(z) = E/g_0$ for the mode. Figures 5a and 5b show the wave function $E(z)$ for $\bar{\lambda} = 1$ and 2, respectively. We note that $E(z)$ curves for $R = 10$ and 30 peak in a region away from the neutral sheet for both the cases of $\bar{\lambda} = 1$ and 2. Further, $E(z)$ values for $R = 10$ and 30 are indistinguishable from each other. However, the shape of $E(z)$ for $R = 1$ is different for different $\bar{\lambda}$; whereas $E(z)$ decreases continuously as Z decreases for $\bar{\lambda} = 1$ (Figure 5a), it peaks in a region away from $z = 0$ for the case of $\bar{\lambda} = 2$ (Figure 5b).

2.2. Inhomogeneous Case

[12] We shall consider the Harris sheet model where the magnetic field and the number density vary as $\mathbf{B} = B_0 \tanh (z/L) \mathbf{x}$, and $n(z) = n_0/\cosh^2 (z/L)$, respectively (cf. Figure 1). For this case, (2) and (3) become

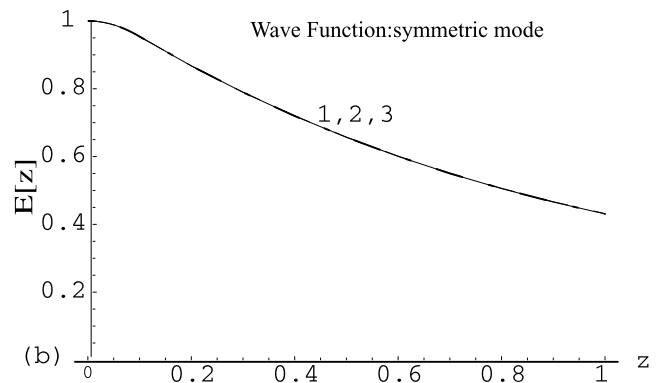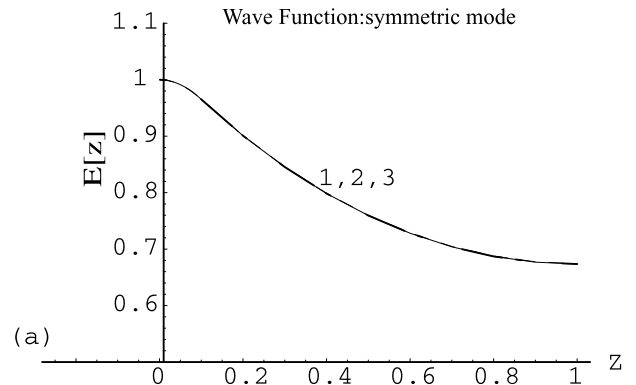$$\frac{d^2 E_1}{dZ^2} - \left[b^2 - \frac{a^2}{\sinh^2 Z}\right] E_1 = 0, \qquad (16)$$

and

$$\frac{d^2 E_2}{dZ^2} - \left[b^2 - \frac{R a}{\cosh^2 Z \tanh Z}\right] E_2 = 0, \qquad (17)$$

On using the transformation $x = \tanh Z$, (16) and (17) can be put in the form

$$x^2 \frac{d^2 E_s}{dx^2} + a_s(x) \cdot x \frac{d E_s}{dx} + b_s(x) E_s = 0, \qquad (18)$$

where the subscript $s = 1$ or 2 for region 1 or 2, respectively, and the coefficients $a_s(x)$ and $b_s(x)$ are given by

Figure 3. Variation of the normalized eigenfunction $E[z] = E/g_0$ (here g_0 is taken as 1) versus normalized distance from the neutral sheet axis $Z = z/L$ for the symmetric mode for $b = 1$, and for the same parameters as in Figure 2; (a) $\bar{\lambda} = 1$ and (b) $\bar{\lambda} = 2$, and curves 1, 2, and 3 are for $R = 1$, 10 and 30, respectively. Note that $E[z]$ does not change appreciably when R is varied from 1 to 30 as the curves for $R = 1$, 10, and 30 get merged into a single solid curve.

(a)

(b)
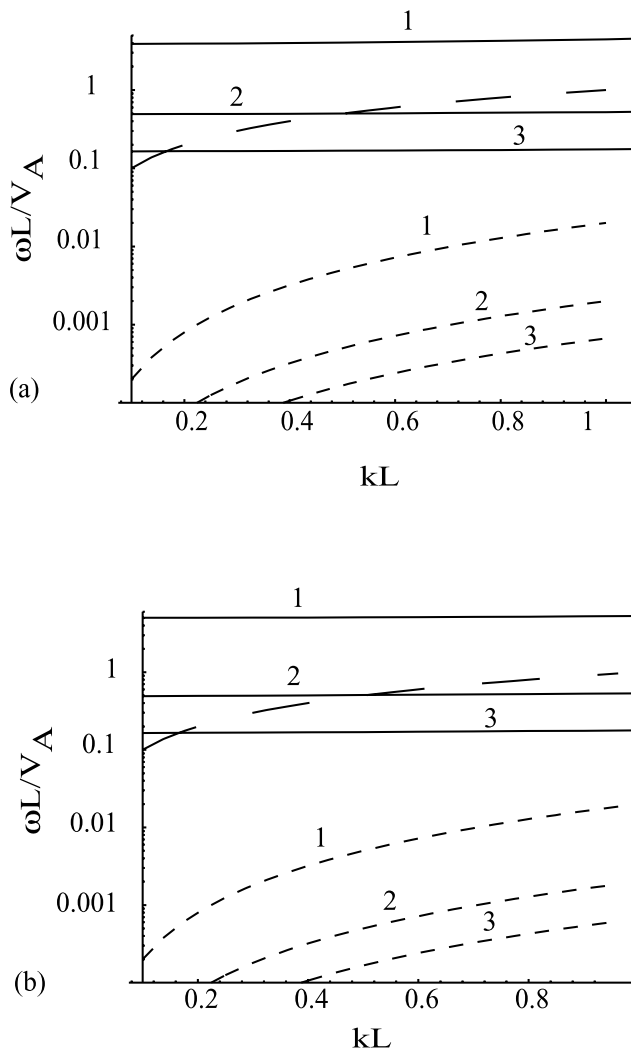
Figure 4. Variation of $a = (\omega L/V_A)$ versus $b = kL$ for the antisymmetric mode in two uniform region case. All the parameters are the same as in Figure 2. Dispersion relation for (a) $\bar{\lambda} = 1$ and (b) $\bar{\lambda} = 2$, and for $R = 1$, 10, and 30. As in Figure 2, dispersion relation for the Alfvén wave, ω_A (the long-dashed curve) and for the helicon mode ω_H, (dashed curves) are also shown. For a given value of R, the frequencies are larger than the corresponding helicon mode frequencies in region 2.

$$a_1(x) = a_2(x) = -\frac{2x^2}{(1-x^2)} \equiv \sum_{k=0}^{\infty} \alpha_k x^k, \tag{19}$$

$$b_1(x) = -\left[\frac{b^2 x^2}{(1-x^2)^2} - \frac{a^2}{(1-x^2)}\right] \equiv \sum_{k=0}^{\infty} \beta_k x^k, \tag{20}$$

and

$$b_2(x) = -\left[\frac{b^2 x^2}{(1-x^2)^2} - \frac{Rax}{(1-x^2)}\right] \equiv \sum_{k=0}^{\infty} \mu_k x^k. \tag{21}$$

Equation (18) can be solved for E_s in both regions 1 and 2 by using the standard method of dealing with regular singular points. Accordingly, we write the solution, say E_1 in region 1 as

$$\phi = x^r \sum_{k=0}^{\infty} c_k x^k, \tag{22}$$

and substitute ϕ in (18) and using (19) and (20), and equating coefficients of various x^k terms to zero, we can find c_ks. Putting the coefficients of the $k = 0$ exponent term yields the indicial polynomial q given by

$$q(r) = r(r-1) + \alpha_0 r + \beta_0 = r(r-1) + a^2, \tag{23}$$

whose two roots, r_1, r_2:

$$r_1 = [1 + (1 - 4a^2)^{1/2}]/2; \quad r_2 = [1 - (1 - 4a^2)^{1/2}]/2, \tag{24}$$

are distinct and whose difference is not an integer number. The $k = 1$ exponent term demands $c_1 = 0$, and it turns out that all odd c_k are zero. The even c_k are obtained from the relation

$$c_k(r) = -\frac{\sum_{j=0}^{k-1} [(j+r)\alpha_{k-j} + \beta_{k-j}]c_j(r)}{q(r+k)}, \quad (k = 2, 4, 6, \cdots). \tag{25}$$

Taking $c_0 = 1$, one can easily construct the series solution for ϕ. Therefore, the solution for E_1 in region 1 can be

(a)

(b)
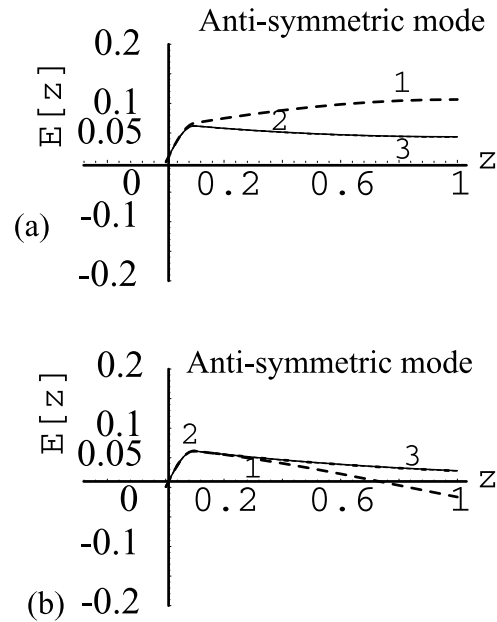
Figure 5. Variation of the normalized eigenfunction $E[z] = E/g_0$ (here g_0 is taken as 1) versus normalized distance from the neutral sheet axis $Z = z/L$ for the antisymmetric mode for $b = 1$, and for the same parameters as in Figure 4. $E[z]$ for (a) $\bar{\lambda} = 1$ and (b) $\bar{\lambda} = 2$, and curves 1, 2, and 3 are for $R = 1$, 10, and 30, respectively. The $E[z]$ does not change appreciably when R is changed from 10 to 30.

Dispersion Relation
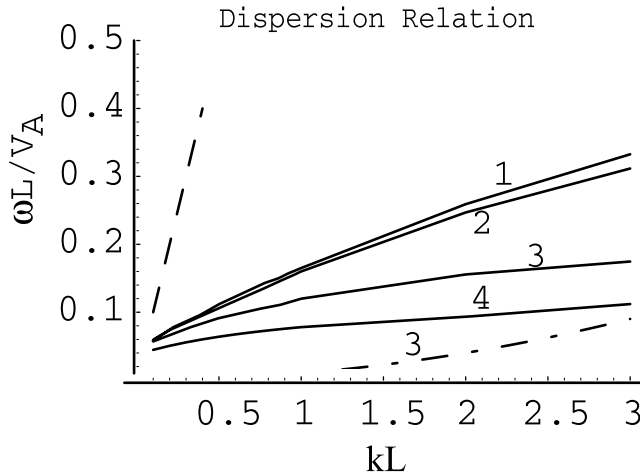
Figure 6. Variation of $a = (\omega L/V_A)$ versus $b = kL$ for the symmetric mode of inhomogeneous case (Harris sheet model) with $\bar{\delta}_i = 0.1$, $\bar{\lambda} = 1$, and for $R = 1, 10, 50$, and 100 for the solid curves 1, 2, 3, and 4, respectively. The long-dashed curve is for the local dispersion relation for the Alfvén mode, ω_A, in region 1 with number density n_0, and the dash-dot-dash curve 3 is for the local dispersion relation for the helicon mode, ω_H, in region 2 for $R = 50$.

written as

$$E_1 = D_1 \, \phi(x, r_1) + D_2 \, \phi(x, r_2), \qquad (26)$$

where

$$
\begin{aligned}
\phi(x, r) &= x^r \sum_{k=0}^{\infty} c_k x^k \\
&= x^r \left[1 + \frac{2r + b^2 - a^2}{q(r+2)} x^2 + \left\{ \frac{2r + 2b^2 - a^2}{q(r+4)} \right. \right. \\
&\quad + \left. \left. \frac{(2r + b^2 - a^2)(2(2+r) + b^2 - a^2)}{q(r+2)q(r+4)} x^4 + O(x^6) \cdots \right\} \right].
\end{aligned}
$$
$$(27)$$

Similarly, the solution for E_2 in region 2 can be written as

$$\psi = x^\rho \sum_{k=0}^{\infty} d_k \, x^k, \qquad (28)$$

and the indicial polynomial p is found to be

$$p(\rho) = \rho(\rho - 1), \qquad (29)$$

whose two roots are $\rho_1 = 1$ and $\rho_2 = 0$. The solution ψ_1, corresponding to the root ρ_1, is found by the same method as described above for ϕ, and the various coefficients d_k can be found by the relation

$$d_k(\rho) = -\frac{\sum_{j=0}^{k-1} [(j + \rho)\alpha_{k-j} + \mu_{k-j}] d_j(\rho)}{p(\rho + k)}, \quad (k = 1, 2, 3, \cdots). \qquad (30)$$

Then, we can write ψ_1 as (with $d_0 = 1$),

$$
\begin{aligned}
\psi_1(x) &= x \left[1 - \frac{R \, a}{p(\rho_1 + 1)} x \right. \\
&\quad + \left. \left\{ \frac{2\rho_1 + b^2}{p(\rho_1 + 2)} + \frac{R \, a}{p(\rho_1 + 1)p(\rho_1 + 2)} \right\} x^2 + \cdots \right].
\end{aligned}
$$
$$(31)$$

Since $\rho_1 - \rho_2 = 1$ integer, the second solution ψ_2 corresponding to the root ρ_2 is given by

$$\psi_2(x) = \sum_{k=0}^{\infty} d'_k(\rho_2) x^k + d \log x \, \psi_1(x), \qquad (32)$$

where

$$d'_k(\rho_2) = \lim_{\rho \to \rho_2} \frac{\partial}{\partial \rho} d_k(\rho), \qquad (33)$$

with $d_0(\rho) = (\rho - \rho_2)$ and $d'_0(\rho_2) = 1$, and d is a constant which may or may not be zero. Then the solution for E_2 in region 2 can be written as

$$
\begin{aligned}
E_2(x) &= G_1 \left[1 + d \, G_2 \log x \right] x \left[1 - \frac{R \, a}{p(\rho_1 + 1)} x \right. \\
&\quad + \left. \left\{ \frac{2\rho_1 + b^2}{p(\rho_1 + 2)} + \frac{R \, a}{p(\rho_1 + 1)p(\rho_1 + 2)} \right\} x^2 + \cdots \right] \\
&\quad + G_2 \sum_{k=0}^{\infty} d'_k(\rho_2) x^k.
\end{aligned}
$$
$$(34)$$

We shall use the following boundary conditions:

$$Z = \bar{\lambda}: \qquad E_1(Z = \bar{\lambda}) = 1; \qquad E'_1(Z = \bar{\lambda}) = 0, \qquad (35)$$

$$Z = 0: \qquad E_2(Z = 0) = 1, \qquad \text{(symmetric mode)}, \qquad (36)$$

and

$$Z = 0: \qquad E_2(Z = 0) = 0, \qquad \text{(antisymmetric mode)}, \qquad (37)$$

along with the matching conditions at $Z = \bar{\delta}_i$:

$$E_1(Z = \bar{\delta}_i) = E_2(Z = \bar{\delta}_i); \qquad E'_1(Z = \bar{\delta}_i) = E'_2(Z = \bar{\delta}_i). \qquad (38)$$

On using the boundary conditions (35)–(36) and the matching conditions (38), we get from (26) and (34) the following complicated dispersion relation for the symmetric mode,

$$
\begin{aligned}
&[\phi'(\tanh \bar{\lambda}, r_2)\phi'(\tanh \bar{\delta}_i, r_1) - \phi'(\tanh \bar{\lambda}, r_1)\phi'(\tanh \bar{\delta}_i, r_2)] \\
&\quad \cdot \psi_1(\tanh \bar{\delta}_i) = [\phi'(\tanh \bar{\lambda}, r_2)\phi(\tanh \bar{\delta}_i, r_1) - \phi'(\tanh \bar{\lambda}, r_1) \\
&\quad \cdot \phi(\tanh \bar{\delta}_i, r_2)] \psi'_1(\tanh \bar{\delta}_i) + [\psi_1(\tanh \bar{\delta}_i)\psi'_2(\tanh \bar{\delta}_i) \\
&\quad - \psi'_1(\tanh \bar{\delta}_i)\psi_2(\tanh \bar{\delta}_i)] \cdot [\phi(\tanh \bar{\lambda}, r_1)\phi'(\tanh \bar{\lambda}, r_2) \\
&\quad - \phi'(\tanh \bar{\lambda}, r_1)\phi(\tanh \bar{\lambda}, r_2)]
\end{aligned}
$$
$$(39)$$

Some numerical solutions of equation (39) are shown in Figure 6 for different values of R. Figure 6 shows that the dispersion relation starts departing from the local dispersion

Wave Function: symmetric mode
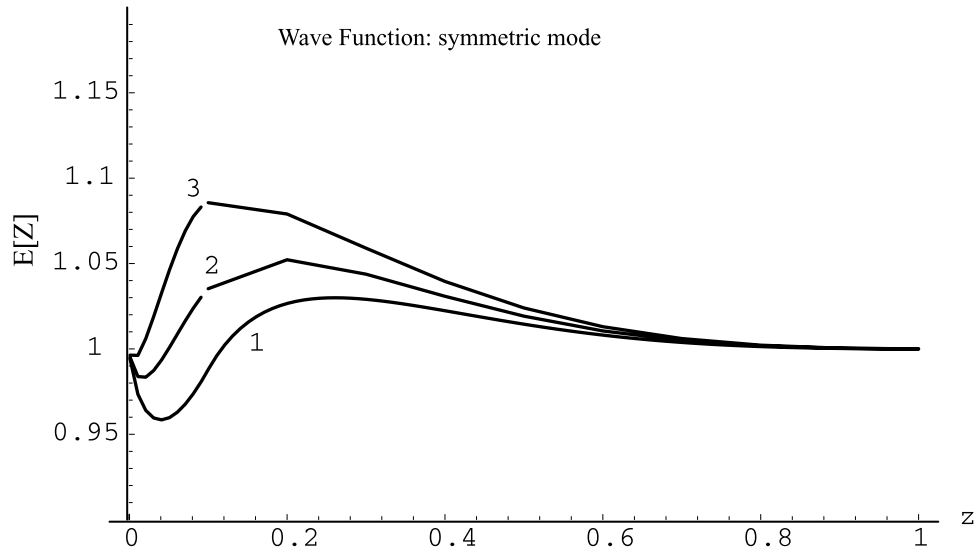
Figure 7. Variation of the eigenfunction $E[z]$ versus normalized distance from the neutral sheet axis $Z = z/L$ for the symmetric mode for $b = 1$, and for $R = 10$, 50, and 100 for curves 1, 2, and 3, respectively. The rest of the parameters are the same as in Figure 6.

relation for the Alfvén wave in region 1 (cf. dashed curve) as well as from the local dispersion relation for the helicon waves in region 2 (dash-dot-dash curve) as R is increased. Figure 7 shows the variations of the normalized wave function $E(z)$ versus z for some values of the parameter R.

[13] Similarly, when the boundary conditions (35) and (37) and the matching conditions (38) are used on (26) and (34), the dispersion relation for the antisymmetric mode can be written as

$$[\phi'(\tanh \bar{\lambda}, r_2)\phi'(\tanh \bar{\delta}_i, r_1) - \phi'(\tanh \bar{\lambda}, r_1)\phi'(\tanh \bar{\delta}_i, r_2)]$$
$$\cdot \psi_1(\tanh \bar{\delta}_i) = [\phi'(\tanh \bar{\lambda}, r_2)\phi(\tanh \bar{\delta}_i, r_1) - \phi'(\tanh \bar{\lambda}, r_1)$$
$$\cdot \phi(\tanh \bar{\delta}_i, r_2)]\,\psi_1'(\tanh \bar{\delta}_i) \qquad (40)$$

Figure 8 shows the dispersion relation for the antisymmetric mode obtained numerically from (40). Once again the eigenvalues are higher than those of the symmetric mode. For larger values of R the dispersion relation behaves differently from that of the local Alfvén modes in region 1 as well as helicon modes in region 2 (dash-dot-dash curve shown for $R = 50$). The behavior of the wave function $E(z)$ is shown in Figure 9.

3. Application to Magnetotail

[14] For the magnetotail, we take the typical values as $B_0 \simeq 25-40$ nT and $n_0 \simeq 0.1-1.0$ cm^{-3}. Then we get the values of the parameter $R \simeq 1-30$ for plasma sheet half-thickness $L \simeq 0.16-1.0$ R_E. If we identify region 2 with the inner central plasma sheet (ICPS) region and the rest of the plasma sheet/lobes as region 1, then we can apply the results of two uniform region case (cf. section 2.1) to this idealized situation.

[15] The assumptions made in the above analysis demand that

$$\Omega_{i2} < \omega < \Omega_{i1} \qquad (41)$$

For the two region case, this means that we have to satisfy the inequalities $1/f_2 < a/R < 1$ simultaneously. For the parameters of Figures 2–5, we have taken $f_2 = 50$, which for $B_0 = 25$ nT (i.e., $\Omega_{i1} = 2.5$ rad s^{-1}), yields $B_2 = 0.5$ nT or $\Omega_{i2} = 0.05$ rad s^{-1}.

[16] We can see from Figure 2 that the symmetric mode can satisfy the inequalities $1/f_2 < a/R < 1$ simultaneously for $R = 1$ for $kL = (0.3-1.0)$(cf. solid curves 1), but not for $R = 10$ and 20 (solid curves 2 and 3). This implies that the symmetric mode can exist for $R = 1-5$ for the parameters of Figure 2. Similarly, we can see from Figure 4 that the antisymmetric mode can satisfy the inequalities $1/f_2 < a/R < 1$ simultaneously for $R = 10$ and $kL = (0.1-1.0)$ (cf. solid curves 2), but not for $R = 1$ and 30 (cf. solid curves 1 and 3). Thus the antisymmetric mode can exist for $R \simeq 8-12$ for the parameters of Figure 4.

[17] We shall consider the case of plasma sheet half-thickness $L = 1000$ km which corresponds to the growth phase of substorms. On taking $n_0 = 0.5$ cm^{-3} as a typical value for the plasma sheet density, we get $V_A \approx 800$ km s^{-1}. Then, the typical frequencies of the symmetric helicon modes are $f_s \sim (1-15)$ mHz with wavelengths (along x direction) in the range of $\sim(0.9-3)$ R_E. The antisymmetric helicon modes will have frequencies $f_{as} \sim (5-80)$ mHz and the wavelengths (along x direction) of $\sim(0.9-9)$ R_E.

[18] For the application of our results for the inhomogeneous case, we note that the magnetic field in region 2 can approximately be written as $B_{i2} \approx B_0 \bar{\delta}_i$. Then the inequality (41) can be expressed in the form

$$\bar{\delta}_i < a/R < 1 \qquad (42)$$

In Figures 6–9, we have taken $\bar{\delta}_i = 0.1$. Then, we find from Figure 6 that in the range $1 < kL < 3$, the symmetric mode satisfies both the inequalities (42) for $R = 1$ (cf. solid curve 1), but not for $R = 10$, 50, and 100 (cf. solid curves 2, 3, and 4). It appears that the symmetric modes could probably exist

Dispersion Relation
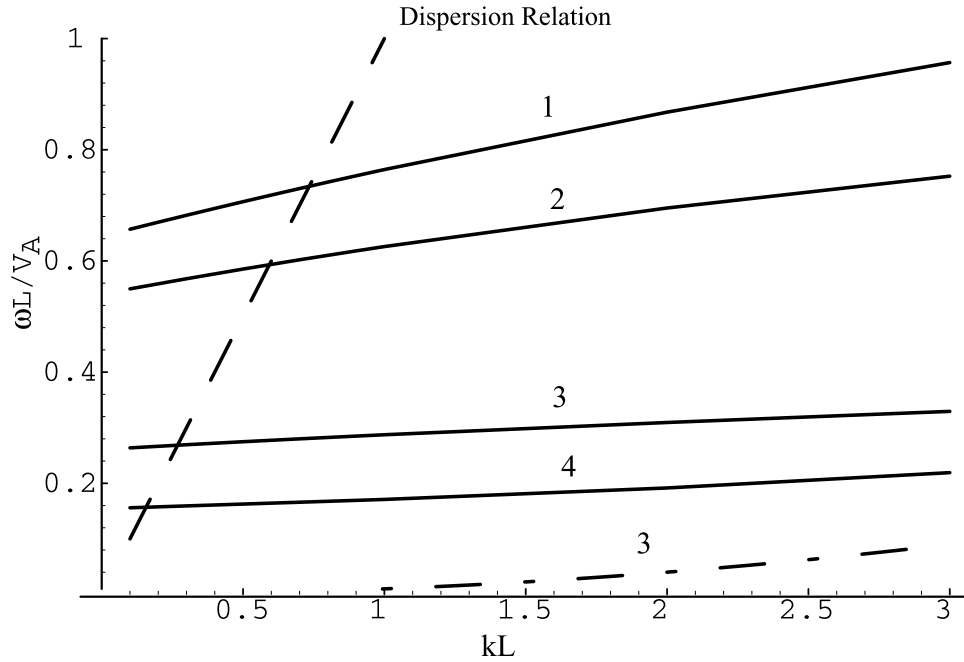
Figure 8. Variation of $a = (\omega L/V_A)$ versus $b = kL$ for the antisymmetric mode of inhomogeneous case (Harris sheet model) for $R = 1$, 10, 50, and 100 for the solid curves 1, 2, 3, and 4, respectively. The long-dashed curve is for the local dispersion relation for the Alfvén mode, ω_A, in region 1 with number density n_0, and the dash-dot-dash curve 3 is for the local dispersion relation for the helicon mode, ω_H, in region 2 for $R = 50$. The rest of the parameters are the same as in Figure 6.

for $R = 1-3$. Similarly, from Figure 8, we find that the antisymmetric modes satisfy the above inequalities for $R = 1$ for $0.1 < kL < 3$ (cf. solid curve 1), but not for $R = 10$, 50, and 100 (cf. curves 2, 3, and 4). The antisymmetric modes can exist in the magnetotail for $R = 1-5$. The reduction of $\bar{\delta}_i$ will further increase the regime of R for both these modes.

[19] Let us also consider $V_A \approx 800$ km s^{-1} for the inhomogeneous case. Then the typical frequencies of the symmetric helicon modes are $f_s \sim (20-50)$ mHz with wavelengths in the x direction of $\sim(0.3-0.9)$ R_E. The typical frequencies of the antisymmetric helicon modes are $f_{as} \sim (50-100)$ mHz. These modes would have wavelengths (along x direction) in the range of $\sim(0.3-9)$ R_E.

[20] From the above discussion it is clear that both the symmetric and antisymmetric modes can exist in the magnetotail. So far, we have discussed the characteristics of the modes in terms of the helicon wave electric field. We can express the helicon wave electric field component in terms of the magnetic field components by using the Faraday law. This gives the helicon wave magnetic field $B = (B_z + iB_y) = (ck/\omega)(E_y - iE_z) = (ck/\omega)E$. Therefore, the characteristics of the eigenfunction of the helicon wave magnetic field will be qualitatively similar to that of helicon wave electric field eigenfunction shown in Figures 2−9. Further, from the boundary conditions for the symmetric modes at $z = 0$, we note that $B(Z = 0) \neq 0$ and $B'(z = 0) = 0$. Therefore, this mode allows the magnetic flux to cross the neutral axis (cf. Figures 3 and 7). On the other hand, for the antisymmetric helicon mode, the boundary conditions at $z = 0$ imply that $B(Z = 0) = 0$ and $B'(z = 0) \neq 0$. Hence, there is a surface current at the neutral axis (because $B'(z = 0) \neq 0$) but no magnetic flux crossing the neutral axis (i.e., $B(Z = 0) = 0$), cf. Figures 5 and 9). Since the symmetric mode requires a

change of magnetic topology, it must involve reconnection. Hence the flux transport across the neutral axis could be achieved by the symmetric mode without specifically exciting the tearing mode instability [*Papadopoulos et al.*, 1994].

[21] It is interesting to note that the importance of Hall currents in the collisionless magnetic reconnection, first pointed out by *Sonnerup* [1979], has been realized with the observations of quadrupolar out-of-plane hall magnetic field signature in the reconnection diffusion region, both in the magnetotail and at the magnetopause, by Wind, Geotail, Polar, and Cluster spacecraft [*Oieroset et al.*, 2001; *Nagai et al.*, 2001; *Mozer et al.*, 2002; *Runov et al.*, 2003]. This has

Wave Function: anti-symmetric mode
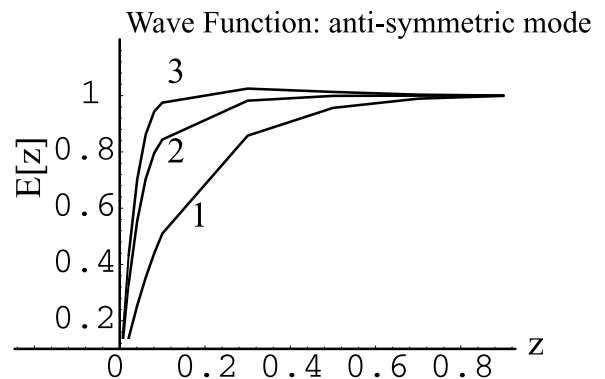
Figure 9. Variation of the eigenfunction $E[z]$ versus normalized distance from the neutral sheet axis $Z = z/L$ for the antisymmetric mode for $b = 1$, and for $R = 10$, 50, and 100 for curves 1, 2 and 3, respectively. The rest of the parameters are the same as in Figure 6.
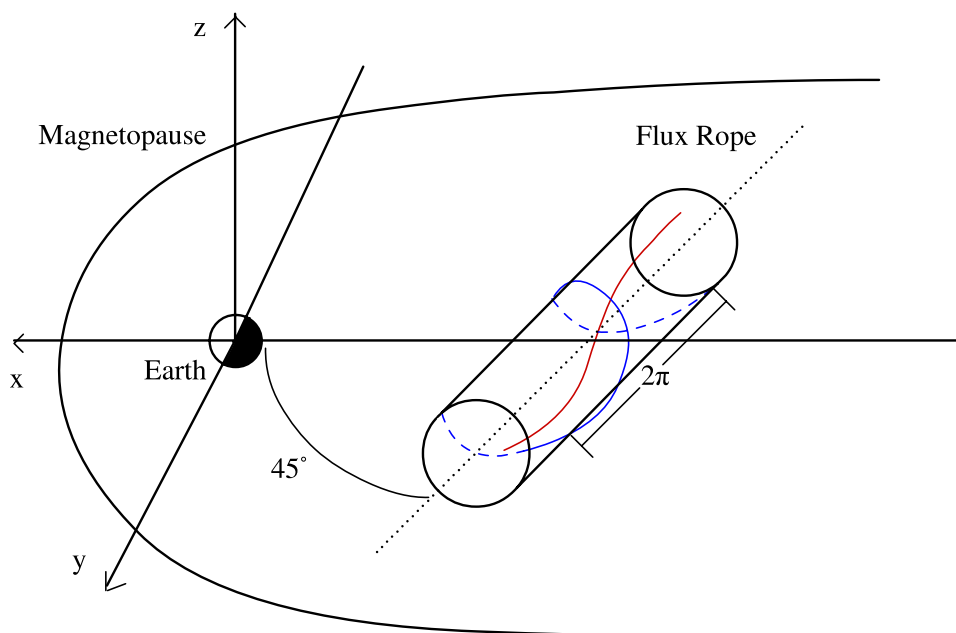
Figure 10. The flux rope structure corresponding to the symmetric helicon mode. The field is maximum on the axis of the rope and decreases radially.

generated a lot of interest in the role of Hall current on the magnetic reconnection process, both in the theory and simulations [*Shay et al.*, 1998; *Morales et al.*, 2005; *Treumann et al.*, 2006]. Since the helicon modes are the natural modes in the plasma supported by the Hall current, they are directly relevant to the magnetic reconnection process.

4. Conclusions

[22] We have studied the helicon modes in the magnetotail for the Harris sheet equilibrium. The plasma sheet is divided into two regions: the outer region (region 1) where both the electrons and the ions are magnetized and the inner region (region 2) where the electrons are treated as magnetized but the ions are unmagnetized. We solve the wave equation for the two cases, namely, (1) where both the regions are treated as uniform but with different plasma parameters and (2) the inhomogeneous case. The wave equation is solved for the symmetric and antisymmetric helicon modes. The antisymmetric mode can exist in a wider range of the parameters than the symmetric helicon mode. Further, the antisymmetric mode does not allow any flux crossing across the neutral sheet axis. On the other hand, the symmetric helicon mode does allow the flux crossing, and thus it must involve reconnection.

[23] The helicon modes are localized global modes propagating mainly along the x axis inside the magnetotail and evanescent beyond the magnetopause. These waves could be excited by two mechanisms. The first is the magnetopause boundary perturbations due to the solar wind as suggested by earlier studies [*Siscoe*, 1969; *Zelenyi and Kuznetsova*, 1984]. In this case, the boundary conditions given by equation (6) simulate the magnetopause perturbations. The second is the current sheet where magnetic field energy is readily converted into plasma energy and can result from instabilities of the plasma.

[24] It is found that the case of uniform regions predicts lower frequencies for both the symmetric and antisymmetric modes than that of the inhomogeneous case. For the typical plasma sheet parameters discussed here, the symmetric helicon modes have frequencies in the range of $\sim(1-50)$ mHz and the antisymmetric helicon modes have frequencies $\sim(5-100)$ mHz. The wavelengths (along x direction) associated with the symmetric and antisymmetric helicon modes are in the range of $\sim(0.3-3)$ R_E and $(0.3-9)$ R_E, respectively. However, depending upon the actual parameters for a given event, the frequency and wavelength ranges could be shorter or broader than the above values. Typically, the wave frequencies would be lower and the wavelengths longer in thicker plasma sheets. Thus, the helicon modes are relevant for the understanding of some of the ULF noise and large magnetic field fluctuations observed near the neutral sheet region at substorm onset [*Russell*, 1972; *Lui et al.*, 1992; *Bauer et al.*, 1995]. Further, the fluctuating B_z component associated with the helicon modes could result in the modulation of the normal component of the background magnetic field. This could provide the electron scattering required for exciting ion tearing mode instability in the magnetotail. This would in turn may trigger large-scale processes at the inner central plasma sheet such as magnetic reconnection and formation of the near-Earth neutral line which is essential for the near-Earth neutral line model of the substorm.

[25] It is worth pointing out that although the treatment given here considers the linear modes, the dispersion relation (1) remains valid even for any arbitrary finite-amplitude right-hand circularly polarized waves as long as the wave propagation is parallel to $\mathbf{B_0}$. Therefore our results are expected to remain valid for finite-amplitude waves also.

[26] The symmetric mode, shown in Figure 3, corresponds to a flux rope, and a schematic diagram is shown in Figure 10. The flux rope [*Slavin et al.*, 2003; *Shen et al.*,

2007] considers a perturbation in the x-y plane with the variation in amplitude in the z direction as in Figure 3, viz. the amplitude has a peak on the axis and decreases with the radial distance. With a perturbation with the same characteristic length in the x and y directions the axis of the rope is oriented as shown in Figure 10. The antisymmetric mode would manifest as twisted flux tubes with embedded strong current sheet.

[27] Furthermore, considering the Harris sheet equilibrium for the geomagnetic tail is an idealization of the real situation. In practice, a finite B_{0z} magnetic field component normal to the current sheet is present, especially for the case of thick ($L \gg \rho_i$) current sheets. However, when the magnetotail is stretched and the plasma sheet becomes thin, the equilibrium B_{0z} can become quite small. The neglect of equilibrium B_{0z} is justified as long as the condition $\rho_i/L \gg (B_{0z}^2/2B_0^2)$ is satisfied. Therefore, the model discussed here is expected to be valid for the thin current sheet conditions.

References

Aigrain, P. (1961), *Proceedings of the International Conference on Semiconductor Physics, Prague, 1960*, 224 pp., Academic, New York.

Bauer, T. M., W. Baumjohann, R. A. Treumann, N. Sckopke, and H. Lühr (1995), Low-frequency waves in the near-Earth plasma sheet, *J. Geophys. Res.*, *100*, 9605–9618.

Dobrowolny, M. (1968), Instability of a neutral sheet, *Il Nuovo Cimento, Ser. B*, *55*, 427–442.

Fruit, G., P. Louarn, A. Tur, and D. LeQuéau (2002a), On the propagation of magnetohydrodynamic perturbations in a Harris-type current sheet: 1. Propagation on discrete modes and signal reconstruction, *J. Geophys. Res.*, *107*(A11), 1411, doi:10.1029/2001JA009212.

Fruit, G., P. Louarn, A. Tur, and D. LeQuéau (2002b), On the propagation of magnetohydrodynamic perturbations in a Harris-type current sheet: 2. Propagation on continuous modes and resonant absorption, *J. Geophys. Res.*, *107*(A11), 1412, doi:10.1029/2001JA009215.

Fruit, G., P. Louarn, E. Budnik, J. A. Sauvaud, C. Jacquey, D. LeQuéau, H. Rème, E. Lucek, A. Balogh, and N. Cornilleau-Wehrlin (2004), On the propagation of low-frequency fluctuations in the plasma sheet: 2. Characteristics of the MHD eigenmodes and physical implications, *J. Geophys. Res.*, *109*, A03217, doi:10.1029/2003JA010229.

Harrold, B. G., C. K. Goertz, R. A. Smith, and P. J. Hansen (1990), Resonant Alfvén wave heating of the plasma sheet boundary layer, *J. Geophys. Res.*, *95*, 15,039–15,046.

Kalra, S., and G. S. Lakhina (1994), Shear flow instabilities in the Earth's plasma sheet region, *Ann. Geophys.*, *12*, 25–32.

Konstantinov, O. A., and V. I. Perel (1960), Possible transmission of electromagnetic waves through a metal in a strong magnetic field, *Sov. Phys. JETP*, *11*, 117.

Lakhina, G. S. (1992), A kinetic theory of driven reconnection in the Earth's magnetotail, *J. Geophys. Res.*, *97*, 2661–2972.

Lakhina, G. S. (2001), Role of helicon modes in the injection of oxygen ions in the ring current, *J. Atmos. Sol. Terr. Phys.*, *63*, 481–487.

Lakhina, G. S., and K. Schindler (1988), The effects of plasma sheet boundary flow and plasma mantle flow on the ion tearing instability, *J. Geophys. Res.*, *93*, 8591–8601.

Lakhina, G. S., and B. T. Tsurutani (1997), Helicon modes driven by ionospheric O$^+$ ions in the plasma sheet region, *Geophys. Res. Lett.*, *24*, 1463–1466.

Lakhina, G. S., E. Hameiri, and M. Mond (1990), Ballooning instability of the Earth's plasma sheet region in the presence of parallel flow, *J. Geophys. Res.*, *95*, 10,441–10,448.

Lee, L. C., S. Wang, C. Q. Wes, and B. T. Tsurutani (1988), Streaming sausage, kink and tearing instabilities in a current sheet with applications to the Earth's magnetotail, *J. Geophys. Res.*, *93*, 7354–7365.

Louarn, P., G. Fruit, E. Budnik, J. A. Sauvaud, C. Jacquey, D. LeQuéau, H. Rème, E. Lucek, and A. Balogh (2004), On the propagation of low-frequency fluctuations in the plasma sheet: 1. Cluster observations and magnetohydrodynamic analysis, *J. Geophys. Res.*, *109*, A03216, doi:10.1029/2003JA010228.

Lui, A. T. Y., R. E. Lopez, B. J. Anderson, K. Takahashi, L. J. Zanetti, R. W. McEntire, T. A. Potemra, D. M. Klumpar, E. M. Greene, and R. Strangeway (1992), Current disruption in the near-Earth neutral sheet region, *J. Geophys. Res.*, *97*, 1461–1480.

McKenzie, J. F. (1970), Hydromagnetic oscillations of the geomagnetic tail and the plasma sheet, *J. Geophys. Res.*, *75*, 5331–5339.

Morales, L. F., S. Dasso, D. O. GOmez, and P. Mininni (2005), Hall effect on magnetic reconnection at the Earth's magnetopause, *J. Atmos. Sol. Terr. Phys.*, *67*, 1821–1826.

Mozer, F. S., S. D. Bale, and T. D. Phan (2002), Evidence of diffused regions at a subsolar magnetopause crossing, *Phys. Rev. Lett.*, *89*, 1–4, 015002.

Nagai, T., I. Shinohara, M. Fujimoto, M. Hoshino, Y. Saito, S. Machida, and T. Mukai (2001), Geotail observations of the Hall current system: Evidence of magnetic reconnection in the magnetotail, *J. Geophys. Res.*, *106*, 25,929–25,949.

Oieroset, M., T. D. Phan, M. Fujimoto, R. P. Lin, and R. P. Lepping (2001), In situ detection of collisionless reconnection in the Earth's magnetotail, *Nature*, *412*, 414–417.

Papadopoulos, K., H. B. Zhou, and A. S. Sharma (1994), The role of helicons in magnetospheric and ionospheric physics, *Comments Plasma Phys. Controlled Fusion*, *15*, 321.

Runov, A., et al. (2003), Current sheet structure near magnetic X-line observed by Cluster, *Geophys. Res. Lett.*, *30*(11), 1579, doi:10.1029/2002GL016730.

Russell, C. T. (1972), Noise in the geomagnetic tail, *Planet. Space Sci.*, *20*, 1541–1553.

Sharma, A. S., et al. (2008), Transient and localized processes in the magnetotail: a review, *Ann. Geophys.*, *26*, 955–1006.

Shay, M., J. F. Drake, R. E. Denton, and D. Biskamp (1998), Structure of the dissipation region during collisionless magnetic reconnection, *J. Geophys. Res.*, *103*, 9165–9176.

Shen, C., X. Li, M. Dunlop, Q. Q. Shi, Z. X. Liu, E. Lucek, and Z. Q. Chen (2007), Magnetic field rotation analysis and the applications, *J. Geophys. Res.*, *112*, A06211, doi:10.1029/2005JA011584.

Siscoe, G. L. (1969), Resonant compressional waves in the geomagnetic tail, *J. Geophys. Res.*, *74*, 6482–6486.

Slavin, J. A., R. P. Lepping, J. Gjerloev, D. H. Fairfield, M. Hesse, C. J. Owen, M. B. Moldwin, T. Nagai, A. Ieda, and T. Mukai (2003), Geotail observations of magnetic flux ropes in the plasma sheet, *J. Geophys. Res.*, *108*(A1), 1015, doi:10.1029/2002JA009557.

Smith, R. A., C. K. Goertz, and W. Grossmann (1986), Thermal catastrophe in the plasma boundary layer, *Geophys. Res. Lett.*, *13*, 1380–1383.

Sonnerup, B. U. Ö. (1979), Magnetic field reconnection, *Solar System Plasma Physics*, vol. 3, edited by L. J. Lanzerotti, C. F. Kennel, and E. N. Parker, pp. 45–108, North-Holland, New York.

Treumann, R. A., C. H. Jaroschek, R. Nakamura, A. Runov, and M. Scholar (2006), The role of the Hall effect in collisionless magnetic reconnection, *Adv. Space Res.*, *38*, 101–111.

Tsurutani, B. T., M. E. Burton, E. J. Smith, and D. E. Jones (1987), Statistical properties of magnetic field fluctuations in the distant plasmasheet, *Planet. Space Sci.*, *35*, 289.

Verheest, F., and G. S. Lakhina (1991), Nonresonant low-frequency instabilities in multibeam plasmas: Applications to cometary environments and plasma sheet boundary layers, *J. Geophys. Res.*, *96*, 7905–7910.

Zelenyi, L., and M. M. Kuznetsova (1984), Large-scale instabilities of the plasma sheet driven by particle fluxes at the boundary of the magnetosphere, *Sov. J. Plasma Phys.*, *10*, 190–194.

Zhou, H. B., K. Papadopoulos, and A. S. Sharma (1996), Electron magnetohydrodynamic response of a plasma to external current pulse, *Phys. Plasmas*, *3*, 1484–1494.

————————————

G. S. Lakhina, Indian Institute of Geomagnetism, Plot 5, Sector 18, New Panvel (W), Navi Mumbai 410 218, India. (lakhina@iigs.iigm.res.in)

K. Papadopoulos and A. S. Sharma, Department of Astronomy, University of Maryland, College Park, MD 20742, USA. (kp@astro.umd.edu; ssh@astro.umd.edu)